Elastic scattering of $p^{\pm}$, $\pi^{\pm}$, and $K^{\pm}$ on protons at high energies and small momentum transfer

R. L. Cool, K. Goulianos, S. L. Segler,* G. Snow, H. Sticker, and S. N. White
The Rockefeller University, New York, New York 10021
(Received 11 June 1981)

We report on a measurement of elastic differential cross sections for $p^{\pm}p$, $\pi^{\pm}p$, and $K^{\pm}p$ at 100 and 200 GeV/c in the range $0.03 < |t| < 0.10$ (GeV/c)^2. Our data display a simple exponential dependence which is consistent with other measurements in this t region or with extrapolations from higher t.

INTRODUCTION

Measurements of the logarithmic slopes of elastic differential cross sections of hadrons at small momentum transfer have helped to illuminate the nature of the Pomeron in the Regge model, to further the understanding of factorization rules, to confront specific models of the structure of hadrons such as the naive quark model, and to test general physics constraints such as unitarity. Recent results[1,2] at high energies indicate that the slopes for $|t| \lesssim 0.04$ (GeV/c)^2 are larger than those obtained by straightforward extrapolations from higher t values.[3,4] These results have potentially important consequences. Roy,[5] for example, has proved that a discontinuous difference between low- and high-t slopes in πp scattering violates unitarity. Thus, accurate data in the intermediate t range could help clarify the situation.

In this paper, we present results for the elastic slope parameters

$$b = \frac{d}{dt} \ln \frac{d\sigma}{dt} \tag{1}$$

from a measurement of elastic and diffractive cross sections of $p^{\pm}$, $\pi^{\pm}$, and $K^{\pm}$ at 100 and 200 GeV/c in the region $0.03 < |t| < 0.10$ (GeV/c)^2.

METHOD AND APPARATUS

The experiment measured the polar angle and the kinetic energy of the recoil proton as well as the charged multiplicity of the final state. The kinetic energy T_p of the proton provides a direct measure of the momentum transfer squared,

$$t = -2M_p T_p . \tag{2}$$

For low values of t, this technique allows the use of a small and simple apparatus with easily defined acceptance. The recoil angle was used to separate out inelastic interactions which did not satisfy the elastic-scattering constraint

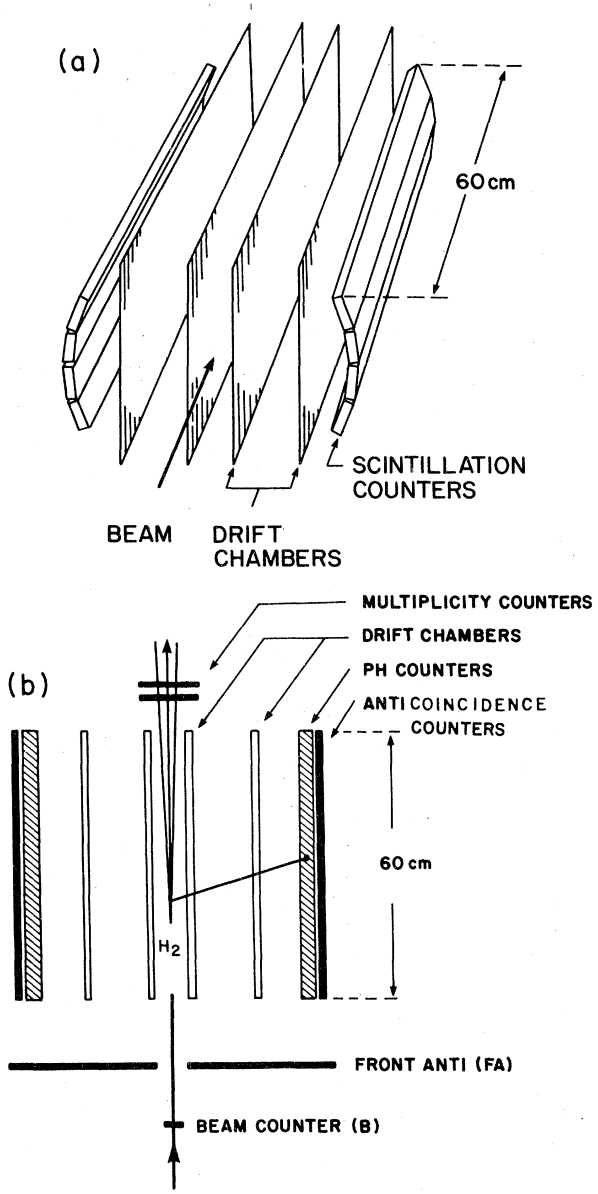

FIG. 1. Recoil detector. (a) View in perspective; (b) plan view.

$$T_p \cong 2M_p \cos^2\theta_p . \quad (3)$$

Other types of background could be kept comfortably low by the additional constraints supplied by the measurement of the charged multiplicity of the final state, the point of interaction along the target, and the time of flight of the recoil particle.

The apparatus, shown in Fig. 1, was situated in the M6W beam line of the Meson Laboratory at Fermilab. A beam momentum of up to 200 GeV/c could be selected with a precision of ±1%. Four Čerenkov counters identified pions, kaons, and protons. Electrons and muons in the beam posed no problem since the minimum recoil energy needed to trigger the apparatus was beyond the region where the Coulomb cross section is important. The target was 40 cm of hydrogen gas at STP. On each side, covering one-third of the solid angle, drift wire chambers (DWC's) measured the position of recoil protons. The energy of the protons was measured by 7.5-cm×60-cm ×2.5-cm-thick Pilot B scintillation counters (PH) which were viewed from both ends by RCA 8575 phototubes. The pulse height and the time relative to the beam counter of each phototube were recorded. Behind the PH counters, anticoincidence counters (A) vetoed protons that did not stop in the PH counters ($T_p > 55$ MeV). The beam was defined by a counter (B) in front of the apparatus while a larger counter (FA) with a hole for the beam vetoed events associated with beam halo. The entire recoil spectrometer could be rotated as well as raised or lowered for calibration with the beam.

The drift chambers consisted of sixteen vertical 5.8-cm-wide cells separated by high-voltage field wires. Other wires with graded potentials established a uniform drift field toward a sense-wire doublet.[6] The doublet could distinguish right from left so that only two drift chambers were needed to define a track, minimizing the amount of material along the path of the recoil proton and consequently the amount of multiple scattering. The space between the drift chambers was filled with hydrogen gas to reduce scattering further. The drift gas, consisting of a mixture of 50% Ar and 50% ethane bubbled through methylal, was separated from the hydrogen regions by thin mylar walls.

The trigger originally was very simple, requiring a coincidence of the beam counters, the drift chambers, the PH counters, and the A counters in anticoincidence. We found, however, that this trigger was dominated by δ rays from the beam. In order to eliminate these δ-ray triggers, we formed a signal from a fast coincidence of short recoil times and low pulse heights, a correlation satisfied only by δ rays, and used it to veto events. This reduced the δ-ray triggers by more than a factor of 10 without affecting the proton recoil triggers. The final trigger $B \cdot \text{DWC} \cdot \text{PH} \cdot \overline{\text{FA}} \cdot A \cdot \bar{\delta}$ resulted in about 60 events per pulse at a 75% live time with a typical beam of 3×10^6 particles per one-second spill.

Two scintillation counters, 6 mm thick and 15 cm in diameter, located 40 cm downstream of the center of the recoil apparatus, were used to measure the charged multiplicity of the final state. In addition, during part of the running, lead-glass blocks were set up 10 m downstream to measure neutral energy and multiplicity. These were not required in the trigger. For the elastic-scattering results reported here, they simply helped to reject inelastic events.

ANALYSIS

The unnormalized differential cross sections were obtained by binning the number of elastic events as a function of t and making small corrections for acceptance and cuts. The proper extraction of elastic cross sections requires good calibration of the angle and energy of the recoil protons and good rejection of inelastic events as well as other types of background.

A. Calibrations

The calibration proceeded in a series of steps. First, the time-distance relations for the DWC's were established from runs in which beam tracks traversed the apparatus in a direction perpendicular to its position during normal running. For this purpose, the apparatus was rotated by 90° and was moved laterally in steps of known amount. The time-distance formulas obtained in this manner were checked by the elastic events themselves, utilizing the direct relationship that exists between time-distance and drift-time distribution when a cell is illuminated uniformly by charged particles.

As a second step in the calibration procedure we determined the angle of the drift chambers relative to the beam. The apparatus was aligned carefully using the rotary table on which it was mounted. The alignment was subsequently checked to within ±0.3 mrad by comparing the angles of elastic recoils on the two sides of the apparatus. The resolution in the measurement of the angle of the recoils was limited by multiple scattering and was typically ±3 mrad.

Calibrating the recoil counters for the kinetic energy of stopping protons as a function of pulse height required a more elaborate procedure. The pulse height varies with the amount of light pro-

duced by the proton, the attenuation of the light in the scintillator, the gain and linearity of the phototube, and the linearity of the analog-to-digital converter (ADC) system. The attenuation of the light in the scintillator was measured by passing the beam through the counters with the apparatus in the rotated position and moving the counters relative to the beam. This also provided the relative gain of the phototubes. The procedure was repeated periodically in order to monitor the gains of the phototubes during each running period and over the eight-month gap between our two running periods. The gain varied by less than a few percent between calibration runs and by less than 10% overall during the entire experiment. Converting light production to energy loss in the scintillator proved more problematic. The standard formula for differential light production is[7]

$$\frac{dL}{dE} = \frac{C}{1 + kB\, dE/dx},$$

where C is an overall constant that can be found from the pulse height of minimum-ionizing particles for which dE/dx is small and kB is a scintillator efficiency parameter whose effect becomes important for recoil protons and is not known precisely enough for our purposes. Published values for kB range from 0.002 to 0.016 g cm^{-2} MeV^{-1}, depending on scintillator type and even on scintillator batch. We therefore found it necessary to evaluate kB from our own data. Starting with a reasonable value of kB, we selected elastic events by requiring charged multiplicity of 1 and by making loose cuts on the calculated missing mass

$$M_X^2 = M_h^2 + 2p_0\sqrt{|t|}\left(\cos\theta - \frac{\sqrt{|t|}}{2M_p}\right). \tag{4}$$

For these events, we then fitted the kinetic energy defined by the angle-energy relation $T = 2M_p \cos^2\theta_p$, treating as free the parameter kB, the phototube gains, and the nonlinearity parameters of the phototubes and of the ADC system. Although these parameters are somewhat correlated, by tightening the cuts and iterating the procedure we obtained stable results with $kB = 0.0082$ g cm^{-2} MeV^{-1}. The energy calibrations are correct to within a systematic uncertainty of $\Delta T = \pm 1$ MeV or $\Delta t = \pm 0.002$ (GeV/c)^2. This is due mostly to kB and the small nonlinearities in the gains of the phototubes. The uncertainty in the absolute angle of the apparatus contributes $\lesssim \pm 0.2$ MeV to the uncertainty in the energy. The resolution in the determination of t is $\sigma_t = 0.002$ (GeV/c)^2.

The multiplicity counters were calibrated using the pulse-height distributions obtained from beam tracks. The effect of the Landau tail at high pulse

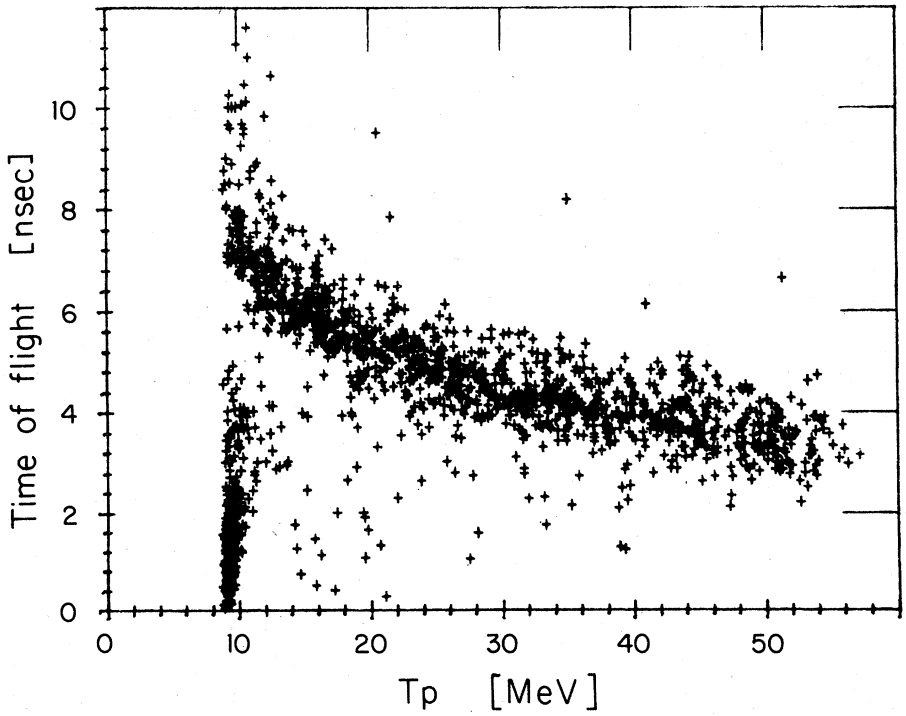

FIG. 2. Time of flight vs energy of recoil particles. The horizontal band represents protons. The events in the lower left corner are mostly due to electrons.

heights was minimized by using only the smaller of the two pulse heights. Finally, the lead-glass blocks were calibrated with muons and electrons. The muons provided a low pulse-height calibration for all blocks while 50 GeV electrons provided a high point for a few selected blocks. Gain stability was checked periodically with muons.

B. Cuts and corrections

The time of flight recorded in each of the two phototubes of a counter was employed in two ways. First, the time difference was converted to a position in the counter, with a resolution of ±0.9 cm, and compared with the position obtained by extrapolation from the DWC's. A cut of ±3.2 cm was made, eliminating accidental events for which the track did not extrapolate to the point of energy deposition in the counter. Then, the average time of the two phototubes relative to the beam counter was compared to that expected for a recoil proton. A scatter plot of time of flight versus kinetic energy is shown in Fig. 2. The prominent band is due to protons; the remaining events are due to accidentals and other recoil particles, mainly electrons and pions. A cut of ±1.2 nsec, corresponding to 3.5σ, was applied around the proton band.

Inelastic events were removed by requiring charged multiplicity of 1. Events with neutral energy in the lead-glass were rejected for runs where such a requirement was applicable, including all the ±200 GeV/c and part of the −100 GeV/c data. Elastic events were then selected by a cut in missing mass squared. Figure 3 shows the M_X^2 distribution for $\pi^- p \to Xp$ at 100 GeV/c. The resolution is $\sigma(M_X^2) = 0.22$ GeV^2 and scales with the beam energy. To avoid introducing a t-dependent bias arising from the cuts, we cut generously at ±1 GeV^2 about the elastic peak for the 100-GeV/c data and ±2 GeV^2 for the 200-GeV/c data.

The elastic events obtained in this manner were corrected for the remaining inelastic contamination (0.3 to 4%), for the geometrical acceptance of the apparatus (≲4%), for multiple scattering of recoil protons from the DWC field-shaping wires (≲2%), and for nuclear interaction of the protons in the scintillator (≲2%).

C. Normalization

For each particle and energy, the data were fitted to the function

$$\frac{d\sigma}{dt} = Ae^{bt} . \tag{5}$$

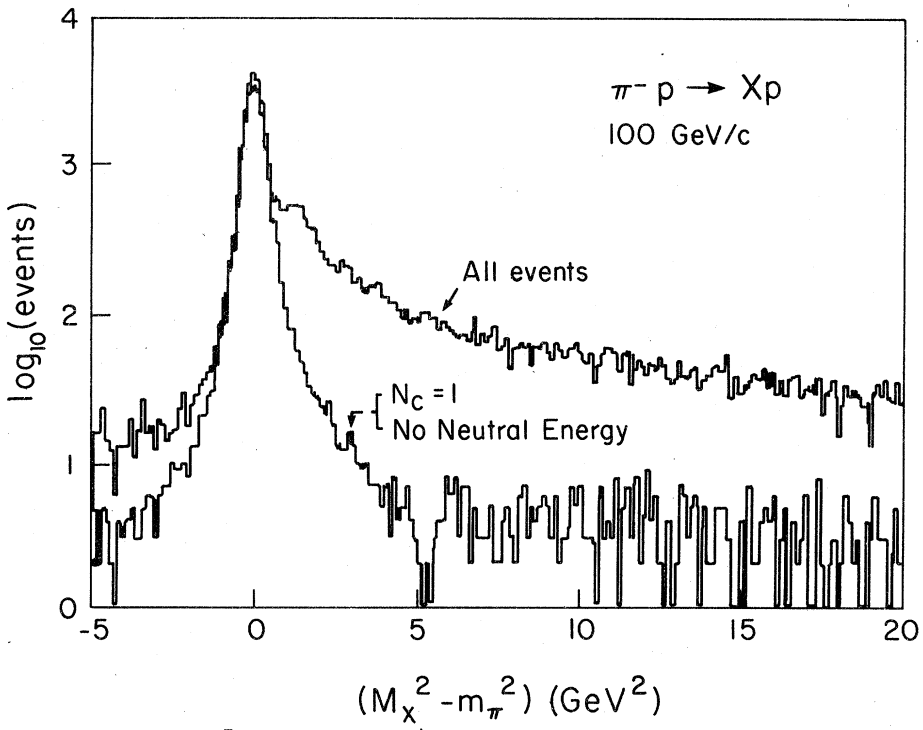

FIG. 3. "Missing mass" plot for $\pi^- p \to Xp$ at 100 GeV/c. The upper histogram contains all the events. The lower histogram represents the (elastic) events remaining after requiring charged multiplicity of 1 and no energy deposited in the lead-glass blocks downstream.

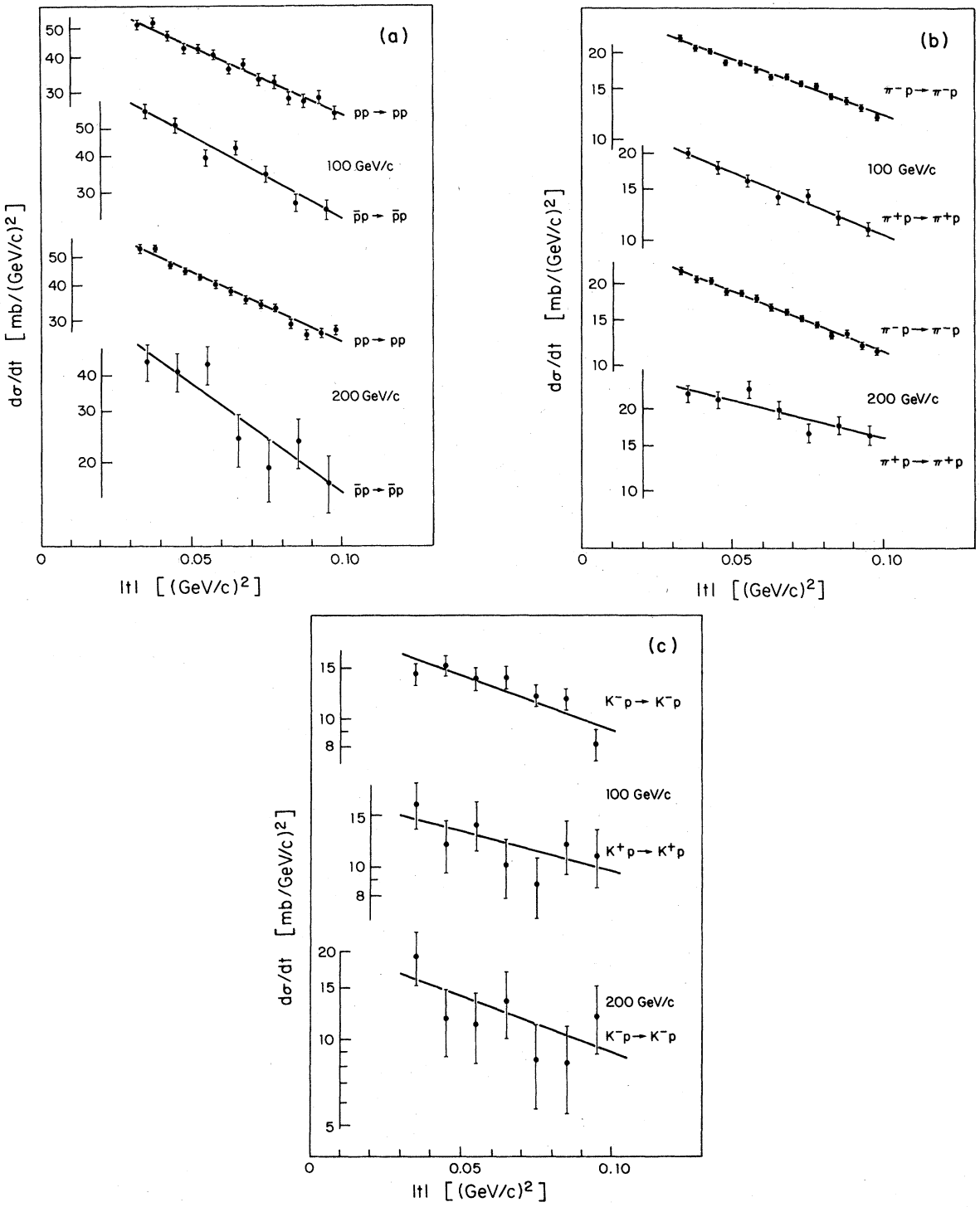

FIG. 4. Elastic differential cross sections as a function of t. (a) pp and $\bar{p}p$ at 100 and 200 GeV/c; (b) $\pi^{\pm}p$ at 100 and 200 GeV/c; (c) $K^{\pm}p$ at 100 GeV/c and $K^{-}p$ at 200 GeV/c.

In principle, the normalization could have been determined from the event rates. However, uncertainties in beam structure, triggering efficiency, dead time, and solid angle limited the accuracy of such a determination to ~20%. For this reason, we normalized our data by scaling

TABLE I. Elastic hadron-proton cross sections $d\sigma/dt$ [in mb $(\mathrm{GeV}/c)^{-2}$] and fits to the form $d\sigma/dt = Ae^{bt}$.

Beam Particle	Beam Energy (GeV)	t value $[(\mathrm{GeV}/c)^2]$	0.03–0.04	0.04–0.05	0.05–0.06	0.06–0.07	0.07–0.08	0.08–0.09	0.09–0.10	A [mb $(\mathrm{GeV}/c)^{-2}$	b $[(\mathrm{GeV}/c)^{-2}]$	χ^2/DF (5 DF)
π^-	100		21.74 ± 0.31	19.38 ± 0.30	17.91 ± 0.29	16.45 ± 0.28	15.44 ± 0.27	13.89 ± 0.25	12.38 ± 0.24	29.43 ± 0.60	8.92 ± 0.31	0.95
	200		21.57 ± 0.37	19.55 ± 0.35	18.21 ± 0.35	16.27 ± 0.33	14.81 ± 0.31	13.29 ± 0.30	12.22 ± 0.28	30.24 ± 0.74	9.55 ± 0.38	0.25
K^-	100		14.2 ± 1.3	15.3 ± 1.3	13.8 ± 1.3	13.9 ± 1.3	11.6 ± 1.1	10.7 ± 1.1	8.2 ± 1.0	21.4 ± 2.6	8.3 ± 1.9	1.2
	200		19.2 ± 3.9	11.7 ± 3.2	11.4 ± 3.1	13.6 ± 3.4	8.5 ± 2.9	8.3 ± 2.8	12.0 ± 3.2	22.0 ± 6.7	9.0 ± 4.8	0.83
$\bar{p}$	100		57.0 ± 3.0	51.1 ± 2.8	39.6 ± 2.5	42.6 ± 2.6	34.4 ± 2.3	27.6 ± 2.1	26.1 ± 2.1	90.6 ± 7.0	13.2 ± 1.2	1.3
	200		44.4 ± 6.5	41.0 ± 6.3	43.6 ± 6.4	23.9 ± 5.0	19.1 ± 4.5	23.3 ± 4.8	16.8 ± 4.1	87.7 ± 19.1	17.0 ± 3.6	1.1
π^+	100		19.97 ± 0.84	17.87 ± 0.80	16.06 ± 0.74	14.12 ± 0.72	14.33 ± 0.72	11.91 ± 0.65	10.95 ± 0.63	27.8 ± 1.7	9.75 ± 0.93	0.56
	200		22.4 ± 1.5	21.5 ± 1.5	23.3 ± 1.5	19.7 ± 1.4	16.4 ± 1.3	17.4 ± 1.3	16.3 ± 1.3	29.0 ± 2.6	6.1 ± 1.4	1.2
K^+	100		16.5 ± 2.9	11.9 ± 2.5	14.0 ± 2.7	10.3 ± 2.3	8.8 ± 2.2	12.1 ± 2.5	11.1 ± 2.4	18.2 ± 4.6	6.2 ± 3.8	0.77
p	100		51.6 ± 1.4	44.7 ± 1.3	41.3 ± 1.2	36.6 ± 1.2	32.7 ± 1.1	28.1 ± 1.0	26.8 ± 1.0	75.6 ± 2.9	11.20 ± 0.60	0.52
	200		53.16 ± 0.93	45.12 ± 0.87	40.98 ± 0.83	36.30 ± 0.78	33.41 ± 0.75	27.65 ± 0.70	27.22 ± 0.67	77.6 ± 2.0	11.50 ± 0.40	2.6

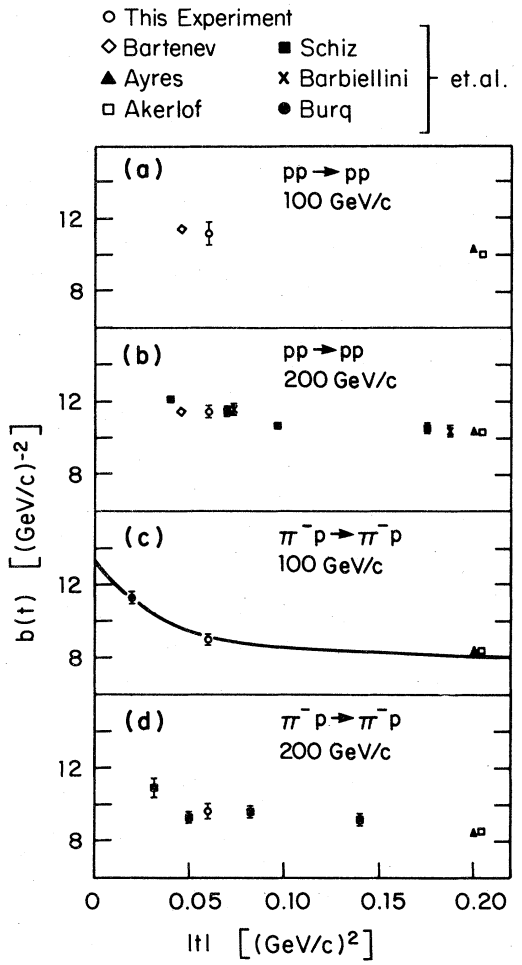

FIG. 5. Elastic slope parameters $b(t)$ as a function of t for pp and $\pi^- p$ at 100 and 200 GeV/c. The line in (c) represents the function $b(t) = d \ln F(t)/dt$, where $F(t)$ is given by Eq. (8) in the text.

A of Eq. (5) to the optical point

$$\frac{d\sigma}{dt}(t=0) = \frac{\sigma_T^2}{16\pi}(1+\rho^2),$$

where σ_T is the total cross section and ρ is the ratio of the real to the imaginary part of the forward scattering amplitude. We set $\rho = 0$, which leads to uncertainties in A of $\lesssim 1\%$, and used the total cross sections of Carroll *et al.*[8] The normalized differential cross sections and the results of the fits are given in Table I.

D. Systematic uncertainties

The errors in Table I are statistical. The uncertainty in the energy scale discussed above in Sec. A contributes a systematic error to the data points of $\Delta\sigma_{el}/\sigma_{el} = b\,\Delta t$. For $b = 10$ $(\mathrm{GeV}/c)^{-2}$ and $\Delta t = \pm 0.002$ $(\mathrm{GeV}/c)^2$, this error is $\pm 2\%$. The sys-

tematic uncertainty in the slopes induced by this error is ± 0.3 $(\mathrm{GeV}/c)^{-2}$.

Since the data are normalized by extrapolating to $t=0$ and scaling to the optical point, the uncertainty in the normalization depends on the form used for the extrapolation and on the uncertainty in the total cross sections ($\Delta\sigma_{el}/\sigma_{el} = 2\Delta\sigma_T/\sigma_T$). The systematic uncertainty in σ_T is[8] $\pm 0.4\%$, resulting to an uncertainty of $\pm 0.8\%$ in the normalization of the elastic cross sections.

Systematic errors due to sources other than the ones already discussed are much smaller. For example, misidentification of hadrons by the Čerenkov counters could lead to shifts in the slopes. However, since the contamination of a hadron by other hadrons due to Čerenkov misidentification was less than 1%, the error in b expected from this source is smaller than $0.01\,\Delta b$, where Δb is the difference in the hadron slopes. For our data, this error is insignificant compared to the error contributed by the uncertainty in the energy.

RESULTS

The simple exponential function (Eq. 5) provides a satisfactory fit to our data (see Table I and Fig. 4). Our slopes are in general agreement with other measurements, as is shown in Fig. 5 which presents compilations of slopes from different experiments[1-4,9] for $pp \to pp$ and $\pi^- p \to \pi^- p$ at 100 and 200 GeV/c. For $\pi^- p \to \pi^- p$, the slopes below our t region are significantly higher than one might expect from a gentle extrapolation of the slopes at higher t. This led Roy[5] to suggest that a break in the slope may exist at $t \cong -0.04$ $(\mathrm{GeV}/c)^2$ which would violate the unitarity bound

$$b(t)\left[\frac{d\sigma}{dt}(t)\right]^{1/2} \geq \frac{b(0)}{2}\left[\frac{d\sigma}{dt}(0)\right]^{1/2}\left[3\frac{(d\sigma/dt)(t_1)}{(d\sigma/dt)(0)}\frac{b^2(t_1)}{b^2(0)} - 1\right], \quad (6)$$

where $t = 3t_1(1 + t_1/4k^2)$ and k is the center-of-mass momentum. A reasonably continuous function $b(t)$ would satisfy the Roy bound.

Our data, combined with other data, are compatible with a continuous function for $b(t)$. For example, Fig. 6 shows our data for $\pi^- p \to \pi^- p$ at 100 GeV/c along with the data of Burq *et al.*[1] and Ayres *et al.*[3] The line through the data represents a fit which uses the full elastic-scattering formula including the Coulomb and interference terms. For the strong-interaction amplitude, a sum of exponentials was assumed,

$$F(t) = N_0[a_1 e^{b_1 t/2} + a_2 e^{b_2 t/2} + (1 - a_1 - a_2)e^{b_3 t/2}]. \quad (7)$$

The relative normalization of the different experiments was allowed to vary within the quoted uncertainty. The result of the fit was

$$F(t) = N_0(0.065e^{39.6t} + 0.649e^{5.3t} + 0.286^{2.4t}), \quad (8)$$

where t is in $(\mathrm{GeV}/c)^2$. The function $b(t) = d\ln F(t)/dt$, drawn in Fig. 5(c), satisfies the unitarity bound (Eq. 6). The same conclusion has been reached by Schiz *et al.*[2]

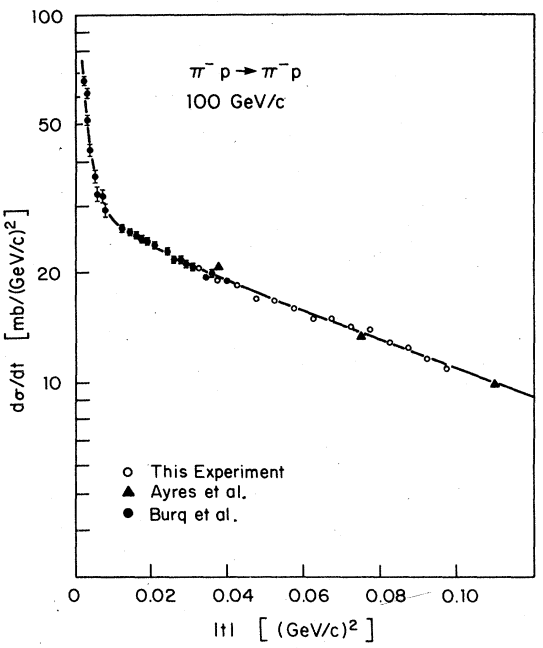

FIG. 6. Elastic differential cross section $d\sigma/dt$ vs t for $\pi^- p$ at 100 GeV/c. The line represents a fit which includes the Coulomb term, the strong-interaction amplitude given by Eq. (7) in the text, and the interference term.

CONCLUSION

We have measured the differential cross sections for $p^{\pm}p$, $\pi^{\pm}p$, and $K^{\pm}p$ at 100 and 200 GeV/c in the range $0.03 < |t| < 0.10$ $(\mathrm{GeV}/c)^2$. In this t range the data display a simple exponential dependence. Our slope parameters are consistent with other measurements in this region and with extrapolations from higher t. Data for $\pi^- p \to \pi^- p$ at lower values of t appear to have significantly higher slopes. A discontinuous break in the differential cross section would violate unitarity. We find that the data can be fitted by a continuous, albeit rapidly changing, function of t that satisfies unitarity constraints.

ACKNOWLEDGMENTS

We wish to thank Guenter Prokesch and Donald Humbert for their invaluable technical help in the construction of the apparatus and the electronics. This research was supported in part by the U.S. Department of Energy.

*Present address: Fermi National Accelerator Laboratory, Batavia, Illinois 60510.

[1]J. P. Burq *et al.*, Phys. Lett. 77B, 438 (1978); Internal Report No. CERN 78-07, EP (unpublished).
[2]A. Schiz *et al.*, Phys. Rev. D 24, 26 (1981).
[3]D. S. Ayres *et al.*, Phys. Rev. D 15, 3105 (1977).
[4]C. W. Akerlof *et al.*, Phys. Rev. D 14, 2864 (1976).
[5]S. M. Roy, Phys. Rev. Lett. 43, 19 (1979).
[6]A. Breskin *et al.*, Nucl. Instrum. Methods 124, 189 (1975); A. Breskin *et al.*, Nucl. Instrum. Methods 119, 9 (1974).
[7]R. L. Craun and D. L. Smith, Nucl. Instrum Methods 80, 239 (1970); J. B. Birks, *The Theory and Practice of Scintillation Counting* (Pergamon, Oxford, 1964).
[8]A. S. Carroll *et al.*, Phys. Lett. 61B, 303 (1976).
[9]G. Barbiellini *et al.*, Phys. Lett. 39B, 663 (1972); V. Bartenev *et al.*, Phys. Rev. Lett. 31, 1088 (1973).